Fractal analysis of 2D and 3D mesocracks in recycled aggregate concrete using X-ray computed tomography images

Xiaoyu Shang[a,b,*], Jingwei Yang[a], Simiao Wang[a], Mingzhong Zhang[c]

[a]School of Civil Engineering and Architecture, Northeast Electric Power University, Jilin, 132012, China

[b]Guangxi Key Laboratory of Disaster Prevention and Engineering Safety, Guangxi University, Nanning, 530000, China

[c]Department of Civil, Environmental & Geomatic Engineering, University College of London, London, WC1E 6BT, UK

Abstract: Recycled aggregates can introduce initial defects and damage to prepared concrete. Internal mesocrack formation is a fatal factor influencing the durable and mechanical properties of recycled aggregate concrete. In this study, the internal mesocracks of recycled aggregate concrete (RAC) under uniaxial compressive loading were virtually and quantitatively investigated by using the X-ray computed tomography (CT) technique. Statistical analysis was conducted on the number, length, width, tortuosity and density of mesocracks in RAC under critically damaged conditions. Then, these mesocracks were numerically extracted and restored to 2D images and 3D structures based on the digital matrix method for fractal geometry analysis. Fractal characteristics and multifractal spectra were used to analyse the mesocrack characteristics of RAC with different recycled coarse aggregate (RCA) replacement rates. The results show that the total number, width, tortuosity and density of mesocracks decrease with increasing RCA replacement rate. The mesocracks inside concrete have self-similarity characteristics, and the corresponding region is a multifractal body. It is feasible to quantitatively characterize mesocrack propagation in the fractal dimension. A clear correlation exists between the fractal dimension and RCA replacement rate: the higher the RCA replacement rate is, the lower the fractal dimension, and the less tortuous the mesocracks. The fractal dimension of mesocracks ranged from 1.19 to 1.32 and 2.18 to 2.39 for 2D images and 3D structures, respectively. Compared with ordinary concrete, the introduction of recycled aggregates leads to a maximum 10 % reduction in fractal dimension. The multifractal spectrum effectively reflects the characteristics of mesocracks at different levels from the local to the global level. Although statistical results indicate that the mesocrack characteristics from 3D structures supply more accurate information than the description from 2D images, mesocracks obtained from 3D structures have fractal characteristics similar to those of 2D images.

Keywords: Statistics analysis; Fractal dimension and multifractal spectrum; 2D image; 3D mesostructure

1. Introduction

The vast consumption of building materials in the construction industry has introduced severe environmental problems. Thus, an increasing number of recycled materials have been developed into building cleaner products in recent years, following “turning waste into treasure”. Waste glass **(Xiao et al., 2020; 2021)**, waste rubber **(Gupta et al., 2019)**, waste wood **(Berger et al., 2020)** and waste ash (**Shang and Li, 2020a**) have been successively reused in novel building materials. Among them, recycled aggregate concrete (RAC) from the reuse of construction and demolition waste, as a typical recycled waste, has been proven to be a feasible and environmentally friendly structural material. However, the issue of whether RAC can be used to completely replace natural concrete is still a concern. In addition, the construction industry lacks confidence in the long-term performance of recycled aggregate products. The unstable property of RAC is also a weakness due to the various resources of the recycled aggregates **(Ouyang et al., 2020)**. As a result, in many laboratories, the performances of RAC have been studied extensively using RCA in different proportions **(Cantero et al., 2020)**, qualities **(Agrela et al., 2021)**, scales **(Oliveira et al., 2020)** and construction methods **(Ahmed et al., 2020)**. Research results have shown that a poor quality of RCA results in weak RAC properties in terms of low apparent density, high water absorption, high porosity, and initial defects from the crushing process **(Wu and Xiao, 2018; Jalilifar and Sajedi, 2020)**. It has been reported that the mechanical and durable properties and bonding with reinforcing steel of RAC are reduced compared with natural aggregate concrete **(Butler et al., 2011)**. However, some studies have shown that the use of high-quality RCA can prevent the performance of RAC from degrading, even better than natural concrete **(Bai et al., 2020; Andreu and Miren, 2014)**. The properties of recycled aggregates from various resources significantly influence the properties of manufactured RAC **(Koper et al., 2017)**. These results indicate that RAC properties are not similar to those of natural concrete, which might obstruct the global involvement of RAC in high-requirement construction.

As mechanical or environmental damage occurs and accumulates, fracture is a fundamental and complex problem for damaged concrete materials, which are related to cracks with various branches. Understanding the process of mesocrack growth is important for analysing the mechanism of dynamic instability in concrete structures and its prevention **(Liu et al., 2011)**. These mesocracks

determine the macromechanical and durable behaviour of the structure. It is widely accepted that the properties of aggregates significantly influence fracture behaviour and crack propagation **(Wei et al., 2020; Kumar and Barai, 2011)**. However, very few studies have quantitively characterized the mesocracks of RCA. The lack of these works is partly due to testing difficulties in accurately and nondestructively capturing interior mesocracks. Moreover, these mesocracks tend to be tiny, irregular and nonuniformly distributed in the matrix. It is also difficult to quantitively describe these mesocracks from the local to the global level. Some current achievements regarding cracks are based on smooth and straight cracks. In fact, real cracks in concrete are complex and exhibit different length, width, tortuosity and density characteristics. These features influence mechanical degradation and durable permeability. Thus, it is important to characterize the geometric parameters of cracks for the evaluation of microproperties.

The nondestructive technique of X-ray CT was developed to provide images of the internal structure of engineering materials from different life domains. The medical CT machine was first introduced to test concrete in the 1980s, and valuable CT images were obtained for aggregates, mortar, and cracks **(Morgan et al., 1980)**. X-ray CT scanning is popular in the field of cement-based materials since it can evaluate 3D microstructures in a nondestructive way compared with other microtesting techniques. A wider application of X-ray CT techniques has been reported in studies on pores **(Han et al., 2018)**, aggregates (**Erdem et al., 2018**), cracks **(Skarżyński., 2019)**, fractures **(Zhang et al., 2016; Huang et al., 2015;)**, damage evolution **(Zhou et al., 2020; Wang et al., 2020)**, microstructure characterization **(Nitka and Tejchman, 2018)** and property evaluation **(Yang et al., 2017)**. Although CT images can be used to reconstruct the 3D structure of materials as a powerful visualization tool for mesostructural analysis, the greyscale values for various phases in cement-based materials are relatively close, and hence, identification of the spatial distribution can be difficult **(Brisarda et al., 2020; Trtik et al., 2013;)**. More recent studies have shown that X-ray CT images combined with simulation tools can enhance the potential for the investigation of complex systems of cement-based materials **(Zhang et al., 2019; Nitka and Tejchman, 2018).**

Mandelbrot introduced fractal geometry theory in 1983 to describe irregular and disordered shapes in nature. Subsequently, **Winslow (1985)** was the first to introduce it into the study of the surface structure of cement paste. **Chiaia et al. (1998)** reported that fractal analysis can capture the variable role of microstructure disorder on the mechanical properties of concrete materials. Some previous scholars **(Saouma et al., 1990; Issa and Hammad, 1993; Carpinteri, 1994)** concluded

that the fractal nature of cracks in concrete materials can be recognized as a pathway to link the roughness of cracks to the fracture toughness of the materials. Subsequently, some researchers tried to use fractal geometry to estimate the mechanical properties of materials by crack characteristics and fracture surfaces **(Xu et al., 2012; Zhang and Wei, 2010)**. **Akhavan et al. (2012)** clarified that proper measurement is of significance for the correct estimation of the fractal behaviour of cracks. Various methods have been adopted to evaluate the fractal dimension of cracks and fracture surfaces, including laser profilometry **(Erdem et al., 2013)**, surface profilometry **(Ficker, 2012)**, crack mapping **(Erdem et al., 2017)**, and X-ray CT scanning **(Liu, et al., 2017; Li et al., 2019)**.

Reviews of RAC indicate that little work has been done to quantitively characterize internal mesocracks and fractal dimensions. This article aims to study the effect of recycled aggregates on RAC mesocracks and to understand the fractal characteristics of mesocracks at different scales. For these purposes, the X-ray CT technique and fractal geometry theory were combined to visually analyse internal mesocracks in RAC. The combination of these two tools provides a powerful method to nondestructively evaluate the spatial characteristics of the mesostructure of RAC. The mesocracks of RAC in critical damage conditions were numerically extracted and restored on two scales of 2D images and 3D structures based on a digital matrix method. Then, statistical analysis was conducted on the geometric characteristics, including the number, length, width, tortuosity and density of mesocracks. The relationship between the mesocrack propagation and the replacement rate of RCA was assessed based on fractal dimension characteristics. A multifractal spectrum was used to further analyse mesocrack propagation. This work aims to provide theoretical and experimental support as well as a fundamental reference for the mesodamage and macrodurability or mechanical property evaluation of RAC.

2. Experimental Procedure

2.1 Materials

Ordinary Portland cement (OPC, CEM I 42.5), fly ash (FA, Class I) and silica fume (SF, Topken 920) were used as the binders. A superplasticizer (Sobute PCA-V) was adopted to adjust the workability. River sand was used as fine aggregate with a fineness modulus of 2.6. Andesite gravel was used as natural coarse aggregate (NCA), with sharp edges and corners and no holes. RCA was produced from construction and demolition concrete wastes. These wastes resources were derived from the deconstruction of 1990s buildings. Original concrete was C30 grade and casted by OPC 32.5 and andesite gravel. After processed by crushing and sieving, uniform RCA containing 5-12 %

residual cement paste by mass was obtained. The physical morphology of NCA and RCA is shown in **Fig. 1**. Table 1 shows the properties of NCA and RCA tested according to **GB/T 14685-2011** and **GB/T 25177-2010.** To avoid the influence of aggregate size on the test results, both NCA and RCA were assigned a continuous grading of 5-16 mm, and particle size distributions conformed to the requirements of **GB/T 14685-2011**. The particle size distributions of binder materials and coarse aggregates are shown in **Fig. 2.**

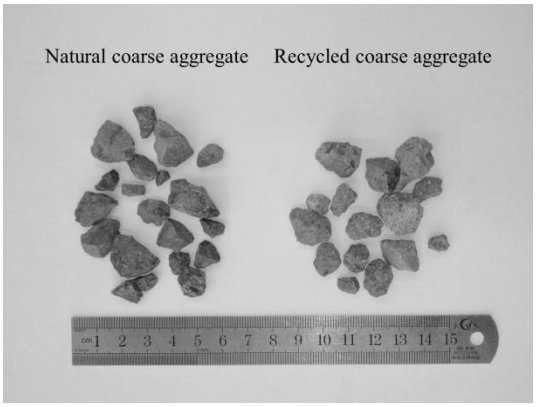

Fig. 1. Morphology of NCA and RCA.

Table 1 Properties of recycled and natural coarse aggregates

Aggregate type	Natural stacking density (kg/m^3)	Porosity (%)	Apparent density (kg/m^3)	Water absorption of 24 h (%)	Crushing index (%)
RCA	1073	56	2425	6.73	20.2
NCA	1479	46	2750	0.57	6.3

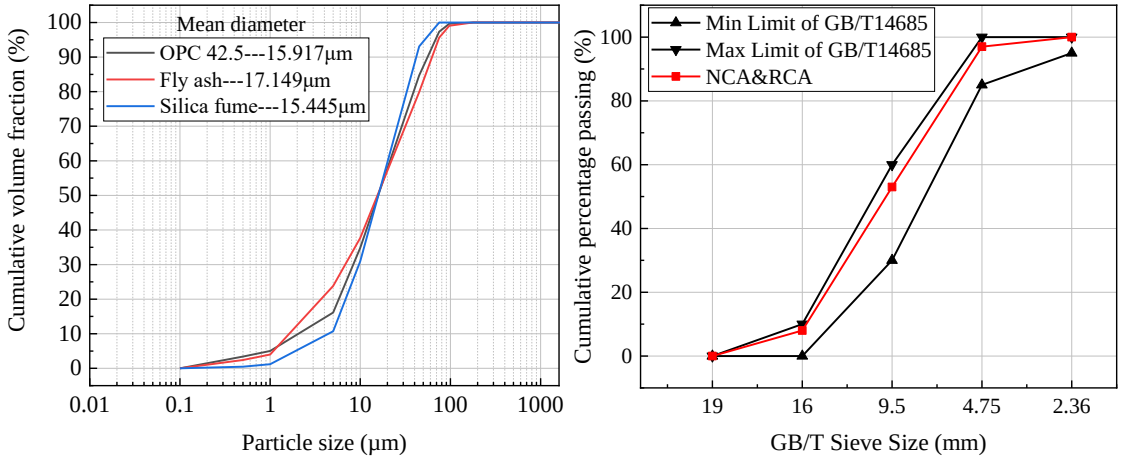

Fig. 2. Particle size distribution of cement, FA, SF, NCA and RCA.

2.2 Mix proportions and samples preparation

Five mixtures of concrete specimens with a strength grade of C30 were designed as part of this research program. The RCA replacement rate (*R* %, mass fraction) was set as 0, 25, 75 and 100 %. The details of the mix proportions are given in **Table 2**. The concrete mixture was mixed and poured into cube moulds with a size of 100 mm×100 mm ×100 mm. The appropriate vibration was

used to densify the materials. After 24 h, the hardened concrete specimens were removed from the moulds and cured to 7 and 28 d in a curing chamber with a temperature of 20 ℃ and relative humidity of 95 %.

Table 2 Mix proportions of recycled aggregate concrete.

Symbol	*R* %	W/B	Mix proportion/(kg/m^3)							
			OPC	Sand	NCA	RCA	Water	FA	SF	Superplasticizer
R0	0	0.50	288	726	1184	0	180	54	18	7.2
R25	25	0.50	288	726	888	296	180	54	18	7.2
R50	50	0.50	288	726	592	592	180	54	18	7.2
R75	75	0.50	288	726	296	888	180	54	18	7.2
R100	100	0.50	288	726	0	1184	180	54	18	7.2

2.3 Uniaxial compression test

A uniaxial compression test was conducted by a universal testing machine (Hualong WAW-1000) according to **GB/T 50081-2002.** The loading was programmed by the combined process of loading and displacement. Initially, loading control was used with a loading rate of 0.5 kN/s until 70 % of the failure load and then changed to displacement control with a loading rate of 0.005 mm/s. Loading finally stopped at 90 % of the failure load. The loading process was strictly controlled to ensure intact cracked specimens for X-ray CT scanning.

2.4 X-ray CT scanning test

A Phoenix v|tome|x s240 microfocus industrial CT machine from GE was used for the CT scanning test, as shown in **Fig. 3(b)**. The parameters of the industrial CT system used in this study were as follows: the industrial CT machine used a cone-beam CT system with 360° rotation scanning, a scanning time of 50 minutes, a rotation of 0.12° per second, a detail resolution of 1 μm, and a maximum tube voltage/power of 240 kV/320 W. The voltage determines the X-ray penetration ability, and the current determines the contrast of different materials in the scanned sample. During scanning, the selection of the appropriate voltage and current is important and depends on the internal density of the sample to ensure clear crack images. In the test program, the scanning parameters were set as a voltage of 190 kV and a current of 110 μA with a tin filter. The dried concrete cube was then placed on the CT scanning platform with its loading side facing up and scanned. The images perpendicular to the loading direction were output images, and in total 1000 CT scanning images with a resolution of 1000×1000 were output with a 0.1 mm interval.

2.5 Mesocrack characterization

All mesocracks were traced to obtain binary images, and tracing work was conducted manually on the enlarged X-ray CT images. From the results, mesocracks can be clearly distinguished from

other porous segments. Although the manual trace for mesocracks costs much more time, it is necessary for accuracy and statistical significance. **Wu et al. (2015)** used a similar method to analyse drying-induced cracks by fluorescence microscopy. In fact, general automated detection is an efficient process but unreliable. For the X-ray CT images, the various phases are separated based on the greyscale value. The accurate identification of such mesocrack phases is difficult, especially for spatial distribution **(Trtik et al., 2013; Brisarda et al., 2020)**. Afterward, these mesocracks were successively extracted and reconstructed following the method for fractal and multifractal calculations. Two scales of 2D images and 3D structures were generated by using a digital matrix method. The original CT image was transformed into a crack and no-crack background with different greyscale values. The crack and noncrack parts were set as 1 and 0, respectively. As a result, a 1000×1000 pixel image was transformed into a binary two-dimensional digital cloud matrix $[A]_{1000\times1000}$, as shown in **Fig. 1**. A method for compressing pixels was adopted to balance the amount of data calculation and details of the structure **(Huang et al., 2015)**. The compressed binary two-dimensional digital cloud matrix $[B]_{256\times256}$ is obtained to display the cracks in 2D images. Furthermore, binary 2D digital cloud matrices $[B_n]_{256\times256}$ are superposed successively from top to bottom by a matrix superposition algorithm. The binary 3D digital cloud matrix $[C]_{256\times256\times256}$ is obtained as mesocracks in 3D structures to describe the spatial distribution.

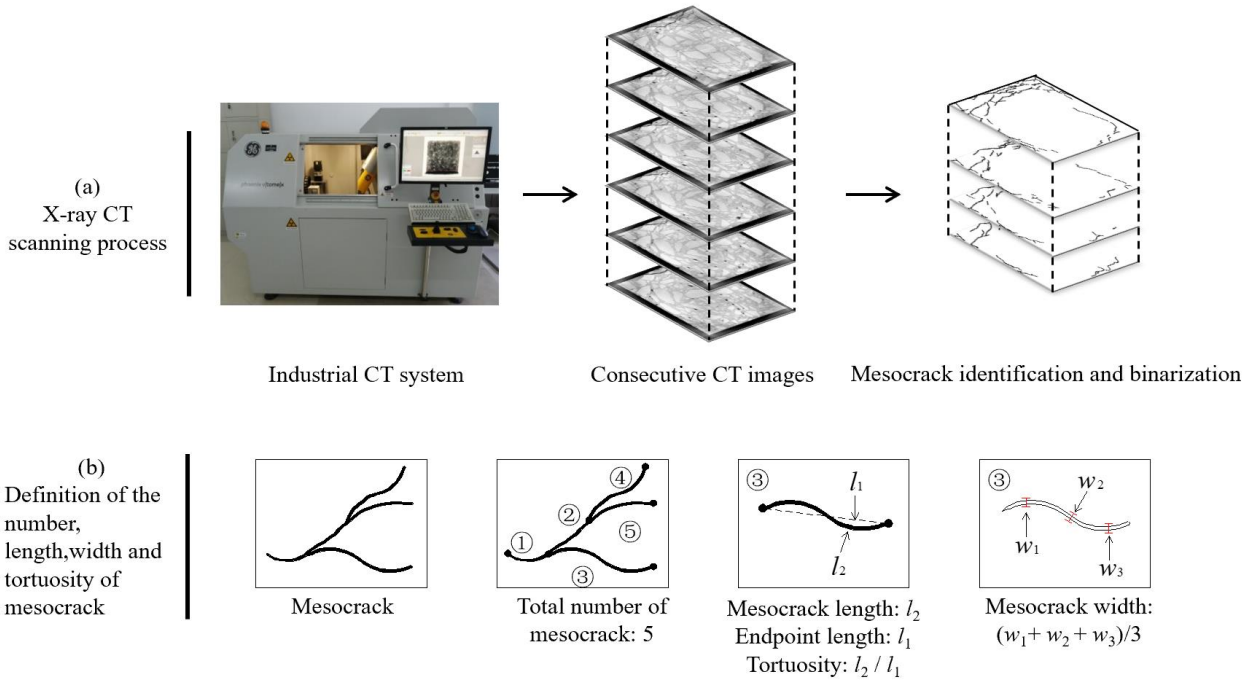

Fig. 3. Acquisition of mesocrack features using X-ray CT: (a) CT scanning process, (b) mesocrack characteristic parameters.

2.6 Statistical method for mesocracks

To analyse the mesocrack failure forms and trends, the number, length, width, tortuosity and density of the mesocracks were calculated by using ImageJ. As shown in **Fig. 3(b)**, a crack was defined between every two ends. There are two types of crack lengths: the endpoint length l_1 and the mesocrack length l_2. l_1 was defined as the distance between the two ends of the crack. l_2 was defined as the actual length. l_1 was used to describe the crack length in this article. Tortuosity was defined as the mesocrack length l_2 divided by the endpoint length l_1. The width was defined as the average of the crack widths w_1, w_2, and w_3 at the three positions of the crack head, middle, and end. Mesocrack density was defined as the percentage of crack pixels in the total pixels of the image.

2.7 Fractal characteristics of mesocracks

Although a statistical analysis of cracks is a good means to analyse the internal failure mechanism, this requires considerable time and calculation and is not efficient. Thus, fractal geometry, including fractal dimension and multifractal spectrum, was introduced to quantitatively characterize the RAC mesocracks. The fractal dimension can describe the whole crack growth and self-similarity of concrete, while a multifractal spectrum can describe the characteristics of different regions in a fractal body from a local point of view and then study the final overall characteristics of the fractal body.

For the fractal dimension calculation, a box dimension method based on MATLAB **(Nayak et al., 2018)** was adopted to calculate the fractal dimension, and the process is shown in **Fig. 4(a)**.

The fractal dimension *D*F can be defined as Eq. (1) **(Falconer, 2003)**:

$$DF = -\lim_{r\to 0} ln\, N\,(r)/\, ln(r) \qquad (1)$$

where F is the fractal body, $N(r)$ is the number of boxes, and r is the side length for the box.

For fractal body F on Rn (N-dimensional space), boxes with side length r cover the area where fractal body F is located. The box is a square in the two-dimensional plane and a cube in the three-dimensional space.

For the multifractal spectrum calculation, square or cube boxes with side length ε are used to cover the crack area. The number of pixels n_{ij} containing cracks in each box (i, j) and the number of pixels $\sum n_{ij}$ containing all cracks in the image are counted. Then, the probability of cracks in each box accounting for the total cracks is obtained. That is a different point from the fractal dimension. Each box in the fractal dimension is represented by presence and absence (1 or 0), while each box in the multifractal spectrum is represented by probability. The probability of crack

distribution $P_{ij}(\varepsilon)$ is calculated by Eq. (2) **(Falconer, 2003)**:

$$P_{ij}(\varepsilon) = \frac{n_{ij}}{\sum n_{ij}} \qquad (2)$$

The crack distribution probability $P_{ij}(\varepsilon)$ and the total number of boxes $N_\alpha(\varepsilon)$ with the same distribution probability have a power function relationship with ε as shown in Eqs. (3) and (4):

$$P_{ij}(\varepsilon) \sim \varepsilon_{ij}^{\alpha} \qquad (3)$$

$$N_\alpha(\varepsilon) \sim \varepsilon^{-f(\alpha)} \qquad (4)$$

where α is the singular index, reflecting the degree of singularity inside each box, $f(\alpha)$ is the fractal dimension of a subset with the same singularity, and the relationship $f(\alpha) - \alpha$ is the multifractal spectrum of cracks.

The statistical method is used to calculate the multifractal spectrum of irregular images. The process is shown in **Fig. 4(b)**.

The partition function $\chi_q(\varepsilon)$ is defined as the sum of the q-th power of the crack distribution probability $P_{ij}(\varepsilon)$, and q is the weight factor:

$$\chi_q(\varepsilon) \equiv \sum P_{ij}(\varepsilon)^q = \varepsilon^{\tau(q)} \qquad (5)$$

Based on Eq. (5), the quality index $\tau(q)$ can be obtained from the slope of the $ln\,\chi_q(\varepsilon) \sim ln\,\varepsilon$ curve:

$$\tau(q) = \lim_{\varepsilon \to 0} \left[\frac{ln\,\chi_q(\varepsilon)}{ln\,\varepsilon} \right] \qquad (6)$$

After the Legendre transformation, the obtained α can be substituted into Eq. (7) to calculate $f(\alpha)$, and then the relation diagram of $f(\alpha) - \alpha$ can be obtained:

$$\alpha = \frac{d[\tau(q)]}{dq} \qquad (7)$$

$$f(\alpha) = \alpha q - \tau(q) \qquad (8)$$

In fact, the multifractal spectrum is a discrete scatter diagram, and α can be obtained from the following formula:

$$\alpha(q) = \frac{\tau(q) - \tau(q - \Delta q)}{\Delta q} \qquad (9)$$

where the range of q is [-50, 50] and the calculation step Δq is 10.

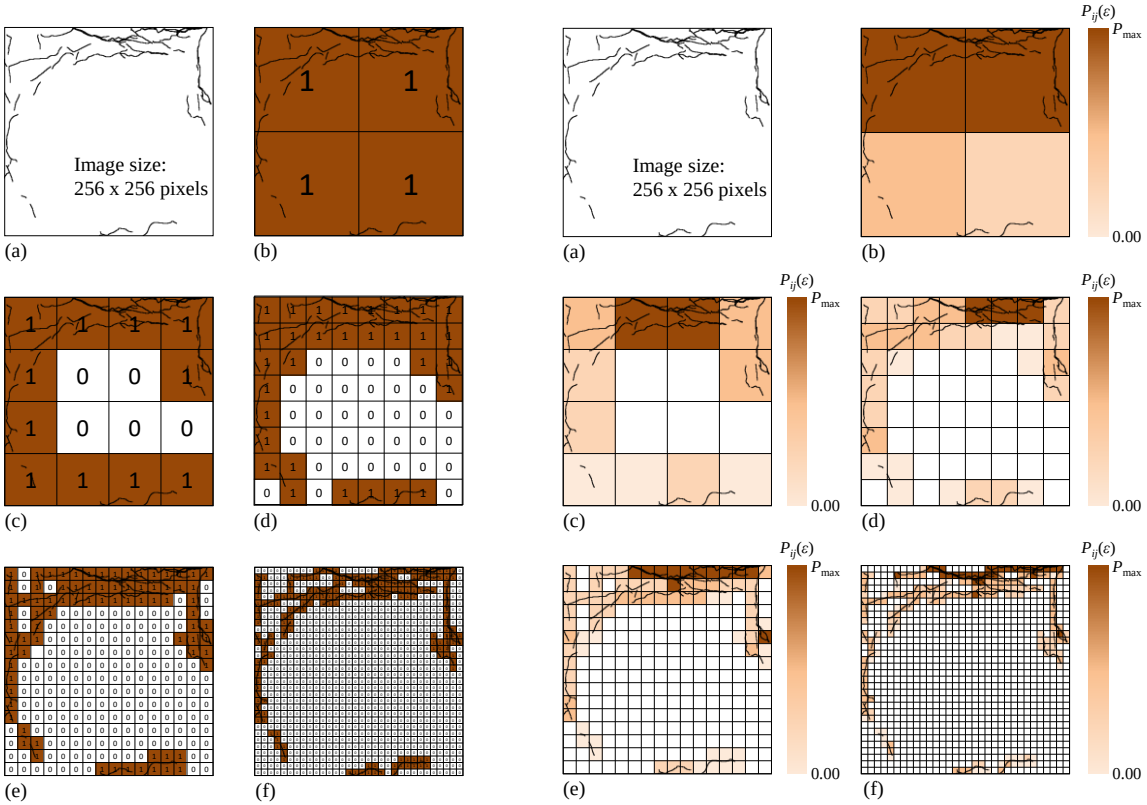

Fig. 4. (A) Box fractal process in the fractal dimension, (B) Box fractal process in the multifractal dimension. (a) 256×256 pixel image; (b) r=256/2=128 pixels; (c) r=256/4=64 pixels; (d) r=256/8=32 pixels; (e) r=256/16=16 pixels; (f) r=256/32=8 pixels.

3. Results

3.1 *Pattern of mesocrack growth*

Fig. 5 shows the X-ray CT 2D images of all concrete samples, which are composed of the aggregates, the cementitious paste, the initial air voids and the growing cracks. The phase with high density tends to be white due to the increased absorption of X-rays. Thus, different composites can be distinguished by the greyscale image. It can be observed that the RCA with various densities resulted in different greyscale values. The quality of CT scanning images was influenced by the amount of RCA due to the similar density. Greyscale natural concrete aggregates indicate the grey cement paste, and the darker shade indicates the recycled concrete aggregates. With approaching failure loading, the cracks spread from the exterior to the interior along the loading direction, and the failure patterns of all concrete samples are cone-shaped. By comparing the images from different positions, a similar mesocrack growth pattern was observed from the top and bottom to the middle, and a small movement close to centre in the middle position was probably due to friction on the loading contact surface. Notably, the mesocrack growth of RAC shows a difference with increasing RCA replacement rate. It can be seen in **Fig. 6** that most natural coarse aggregates had

not been cracked, and some RCA had been cracked through. The types of aggregates influence the development of cracks **(Erdem and Blankson, 2013; Jayasuriya et al., 2021)**. Mesocracks occur in two different positions: in the paste-aggregate interfacial transition zone (ITZ) and through the aggregates.

The nature of the ITZ may be responsible for the decrease/increase in the overall mechanical performance of the mixtures **(Nežerka el al., 2019)**. For ordinary concrete R0, failure cracks mainly developed along the ITZ between the aggregates and cement paste. More possible mesocracks grew to search for the weak area to release energy. The failure pattern changed with the addition of RCA for R25-R100. Mesocrack paths develop either along the ITZ between aggregates and cement paste when encountering a high-strength RCA or through aggregates when encountering a low-strength RCA. Failure through aggregates is possible for RAC so that increased paste strength is not as significant for the mix properties. Similar visual observations have been reported in limestone concrete **(Erdem and Blankson, 2013)**. As the RCA replacement rate increases, the number of mesocrack branches decreases, such as oblique cracks, and only horizontal cracks remain on the development path. RAC samples present a decrease in the size of the cracking zone. This phenomenon is further demonstrated by mesocracks at spatial scales, as shown in **Fig. 6**, where mesocrack growth in 3D structures tends to be monotonous with the increasing RAC replacement rate at spatial scales. **Casuccio et al. (2008)** also found a similar phenomenon for RAC subjected to flexural and uniaxial compression loading. The failure crack morphology for ordinary concrete is mainly affected by the bonding strength of the ITZ **(Golewski, 2018)**. The RAC depends not only on the bonding strength of the ITZ but also on the strength of the RCA.

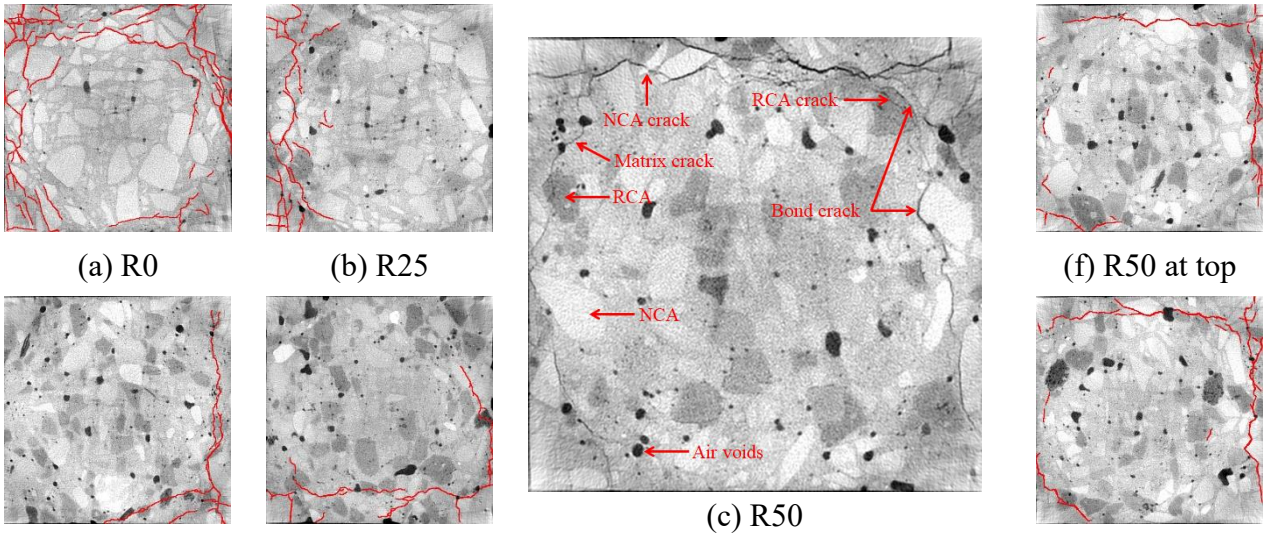

(a) R0 (b) R25 (c) R50 (f) R50 at top

(d) R75 (e) R100 (g) R50 at bottom position

Fig. 5. X-ray CT 2D images of concrete samples at failure

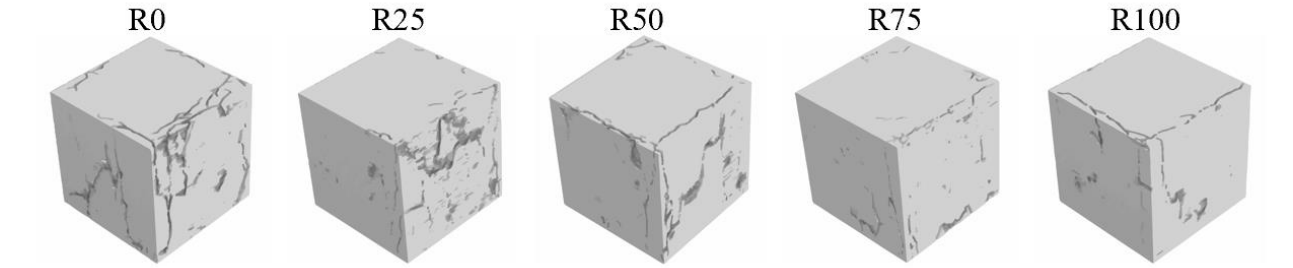

Fig. 6. X-ray CT 3D structures of concrete samples at failure

3.2 *Statistical characteristics of mesocracks*

Figs. 7-9 describe the influence of the RCA replacement rate on the mesocrack characteristics. The crack length, width and tortuosity range from 1.023 to 87.977 mm, 1.05 to 1.627 mm, and 1 to 3.8804, respectively. As seen in **Fig. 7**, crack lengths in the range of 0-20 mm accounted for more than 90 % of all crack lengths for ordinary concrete. The value decreased to less than 80 % when the RCA replacement rate reached 100 %. The average crack lengths increased from 9.540 to 15.563 mm when the RA replacement rate reached 100 %. The same phenomenon was observed in crack width, as shown in **Fig. 8**. Although the crack width showed some fluctuations in the range of less than 0.3 mm, the cracks of ordinary concrete tended to be thick, while the cracks of RAC were relatively thin. The average widths of the cracks gradually decreased from 0.4305 mm to 0.3882 mm, 0.3751 mm, 0.3462 mm and 0.3234 mm with increasing RCA replacement rate. In the width range of 0.1 mm-0.3 mm, fewer thin cracks may not cause obvious changes to the average width. For the tortuosity characteristics of cracks, a value of 1.0 means that cracks form a straight line. A larger tortuosity value means a more fluctuating development path. In **Fig. 9**, it can be seen that 90 % of the crack tortuosity is in the range of 1 and 1.5, and the average tortuosity of cracks from R0 to R100 is 1.2046, 1.1734, 1.1465, 1.0970 and 1.0911. **Fig. 10** shows the mesocrack density of 2D images and 3D structures. The mesocracks account for approximately 1-5 % of the space of RAC, and the mesocrack densities for 2D images and 3D structures are relatively close. However, some apparent differences were observed in the R25 and R75 samples, whose densities from 2D images to 3D structures increased by 40.6 % and 56.3 %, respectively. This indicates that mesocrack characteristics in three dimensions can probably supply more accurate information compared to the description in two dimensions. **Table 3** shows that the number of cracks sharply decreased from R0 to R100. The RCA replacement rate has a cumulative effect on the failure of RAC based on the statistical number of cracks. R0 is the first stage, R25-R50 is the second stage, and R75-R100 is the

third stage. The existence of accumulation effects can also be seen from the crack length, width and curvature ratio distribution diagrams, and this trend is also evident in the fractal and multifractal analysis.

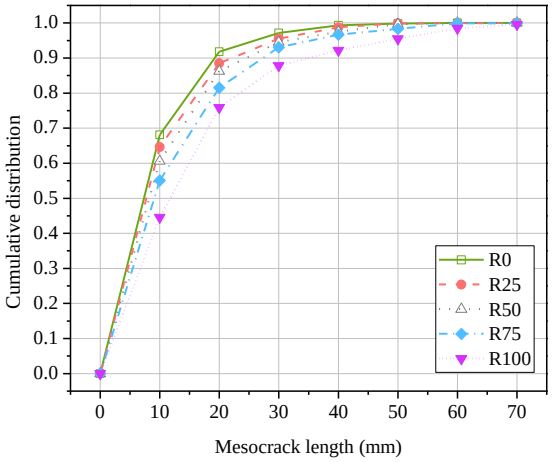

Fig. 7. Effect of RCA replacement rate on length of mesocracks

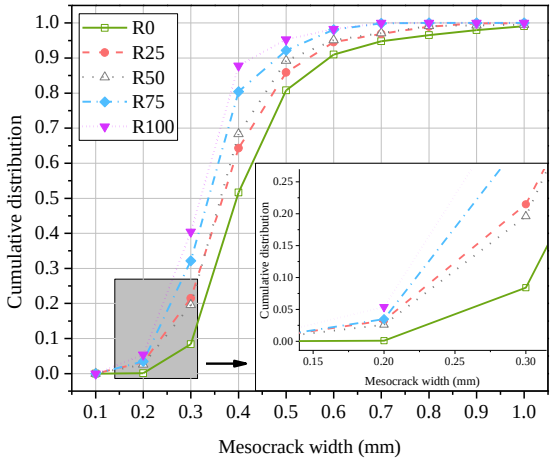

Fig. 8. Effect of RCA replacement rate on width of mesocracks.

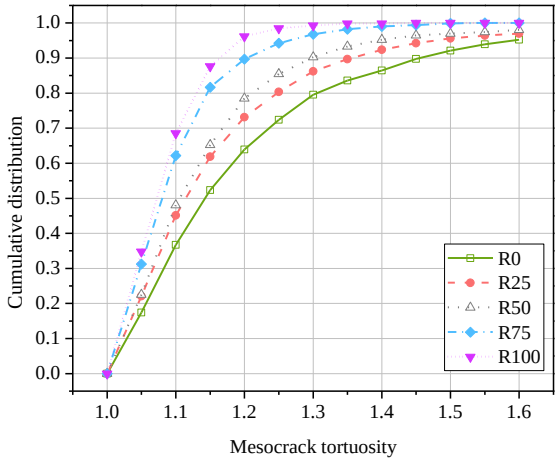

Fig. 9. Effect of RCA replacement rate on tortuosity of mesocracks

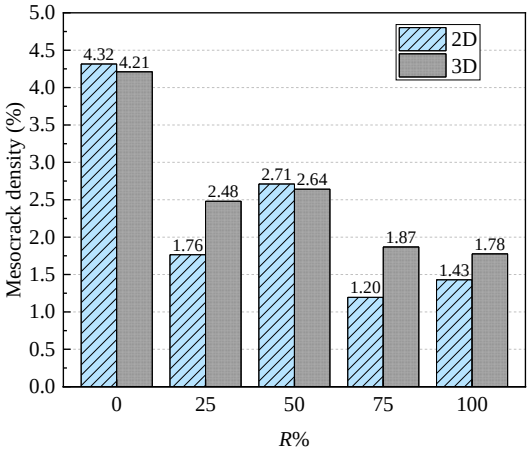

Fig. 10. Effect of RCA replacement rate on density of mesocracks.

Table 3. Statistical characteristics of mesocracks measured from 2D images and the total pixel numbers of 3D mesocracks.

Sample	Number of cracks	Average length (mm)	Average width (mm)	Total area (mm^2)	Total pixel
R0	2129	9.540±0.159	0.4305±0.0031	8743.7	706425
R25	1685	9.420±0.215	0.3882±0.0030	6184.7	416039
R50	1505	10.508±0.253	0.3751±0.0034	5932.0	443039
R75	833	12.414±0.383	0.3462±0.0033	3580.0	313364
R100	705	15.563±0.478	0.3234±0.0032	3549.3	297856

3.3 Fractal characteristics of mesocracks

From the ln$N(r)$-ln(r) fitting curves (Fig. 11), both the 2D images and 3D structure show self-similar characteristics of fractal bodies at different scales. This indicates that the fractal dimensions based on either 2D images or 3D structures can well reflect mesocrack growth. It is thus feasible to quantitatively characterize the failure mesocracks by the fractal dimension.

The fractal dimension is related to surface morphologic complexity and disorder, with a more complex image surface having a higher fractal dimension **(Tian and Han, 2018)**. Fig. 12 shows fractal dimensions of mesocracks in 2D images and 3D structures. Overall, the fractal dimensions in 2D images and 3D structures decrease with increasing RCA replacement rate. In other words, a higher RCA results in a lower fractal dimension of interior mesocracks for RAC, with fewer tortuose cracks. This fact is consistent with the increase in brittleness observed in concretes having aggregates with both improved ITZ and elastic compatibility within paste and aggregates **(Casuccio et al., 2008)**. The rich growth in mesocracks resulted in an increase in the fractal dimension. From the fractal dimension shown in Fig. 12, there are three typical stages with various RCA replacement rates: R0, R25-R50 and R75-R100, which is in accordance with the statistical results. The accumulation effect of RCA influences mesocrack characteristics. In the 2D images, the average mesocrack fractal dimension of the ordinary concrete is 1.32, which decreases to 1.30, 1.28, 1.15 and 1.19 when NCA is replaced by RCA. Different crack patterns result in a decrease in the fractal dimension. The fractal dimension variation trend in the 3D structure is similar to that in the 2D images. The fractal dimensions calculated from the 3D structure are 2.39, 2.26, 2.27, 2.22, and 2.18 from R0 to R100. The same drop occurred with NCA replaced by RCA. Compared with ordinary concrete R0, the fractal dimensions of R25-R100 decrease by 1.25 %, 2.97 %, 12.24 % and 9.58 %, respectively. Notably, the fractal dimension from 3D structures is higher than the fractal dimension from 2D images by approximately 1.0, as shown in **Fig. 12**. **Lange et al. (1993)** also reported that the value of the factual dimension of cement paste obtained from area-based methods is 1 higher

than the value obtained from volume-based methods.

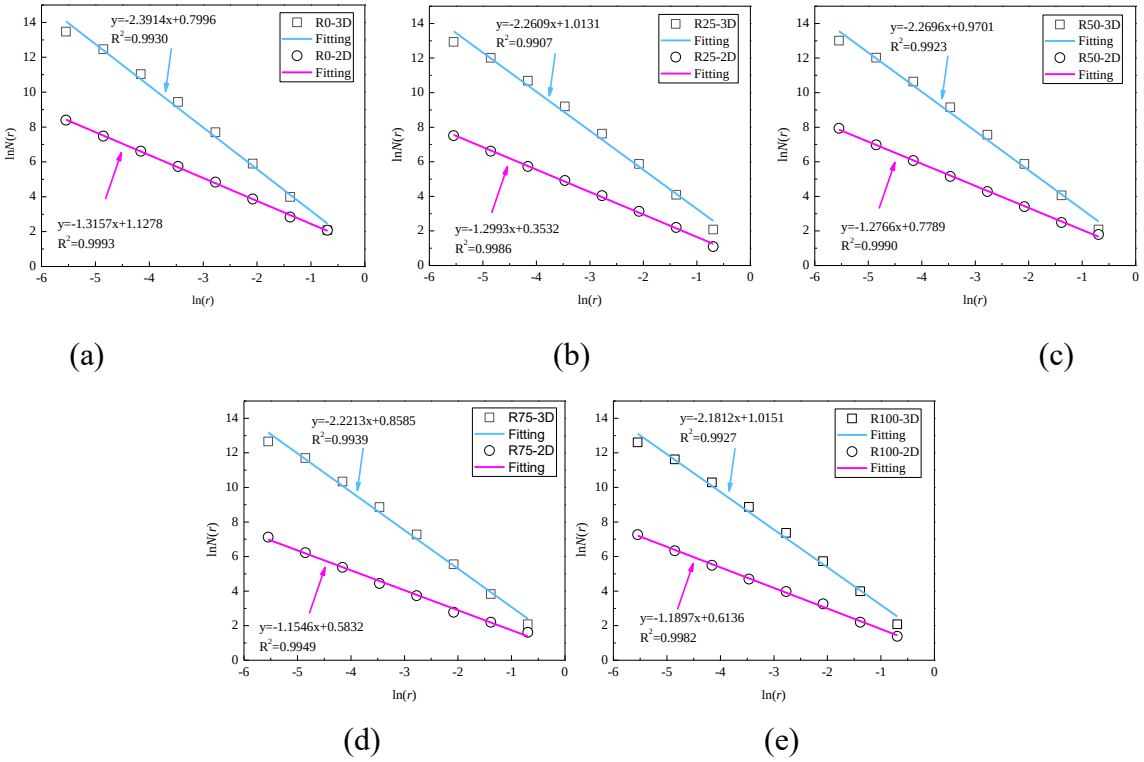

Fig. 11. ln$N(r)$-ln$r$ curves

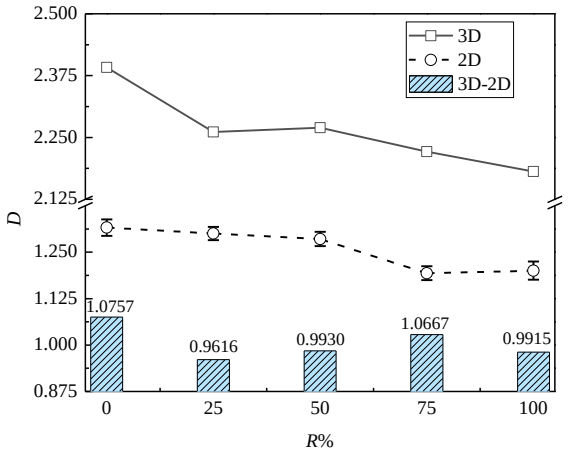

Fig. 12. Fractal dimension of mesocracks in concretes with different RCA replacement rates

3.4 Multifractal characteristics of meso-cracks

Fig. 13 shows the 2D and 3D ln$\chi_q(\varepsilon)$-lnε curve clusters of mesocracks in 2D images and 3D structures. As the q-power increases or decreases, the mesocrack area for each part of the 2D and 3D models can meet the self-similarity characteristics of each scale to a certain extent. In the range of $0< q <50$, the lnχq(ε)-lnε curves show a good linear relationship. However, nonlinearity is obviously enhanced in the range of $-50< q <0$. The nonlinearity from 3D structures is greater than that from 2D images in the upper half part, which means lower scale invariance for mesocracks from 3D structures. Thus, two segments were divided and labelled ①-②, ③-④ as shown in **Fig. 13**. According to the box fractal process, R100-2D and R100-3D show similarity in box sizes of 4-8

and 16-256, 4-32 and 64-256, respectively. This similarity in multisegment scale ranges may occur due to possible poor multifractal characteristics. Although it belongs to an approximate self-similarity as Falconer's definition **(Falconer, 2003)**, 2D and 3D microcracks conform to the multifractal body. A similar phenomenon was reported by **Tarquis et al. (2009) and Liu et al. (2021)** when researching soil pores. The calculated $\log\chi_q(\varepsilon)$-$\log\varepsilon$ curve was divided into two sections, and approximate similarity was maintained in each section. Thus, it is feasible to quantitatively describe 2D and 3D microcracks.

Fig. 14 shows the multifractal spectrum for the mesocracks of concretes with various RCA replacement rates (R) in the 2D image and 3D structure. Significant differences are observed among the mesocracks with varying RCA replacement rates. As described, the multifractal spectrum reflects the information about the mesocrack spatial arrangement. As the RCA replacement rates increase, fewer cracks and less tortuosity cause the multifractal spectrum to move to low α zones. Two important indicators, $\Delta\alpha$ and $\Delta f(\alpha)$, were used to describe the multifractal characteristics of the mesocracks. The specific values are shown in **Fig. 15**. The values of α_{min} and α_{max} reflect the most and least mesocracks in the local area with maximum and minimum probability subsets. $\Delta\alpha$ describes the distribution characteristics of mesocracks. A smaller value of $\Delta\alpha$ indicates more uniform crack growth and a smaller expansion range. The value $f(\alpha_{max})$ reflects the number of boxes of the maximum and minimum probability fractal subsets. A larger $|\Delta f(\alpha)|$ means a more complicated crack texture. $f(\alpha)_{max}$ reflects the crack propagation degree in the entire image. A larger $f(\alpha)_{max}$ means wider and richer crack propagation. **Fig. 14** shows that the multifractal spectra of 2D and 3D mesocracks decrease from R0 to R100. This means that the number of main and branch cracks in the local area decreases and the complexity of cracks weakens with the increasing RCA replacement rate. Compared with 2D image mesocracks **(Fig. 14a)**, the expansion range from the multifractal spectrum from 3D structure mesocracks **(Fig. 14b)** becomes narrow with decreasing $\Delta\alpha$. The range of crack propagation became small. This might be because 3D structures contain more information about mesocracks. As a result, the values of multifractal indicators from 3D structures are also greater than 2D images, as shown in **Fig. 15**. It can also be seen that the multifractal spectrum indicators $\Delta\alpha$ and $|\Delta f(\alpha)|$ of mesocracks have a certain linear relationship with the replacement rate of RCA, which indicates that the multifractal indicators of mesocracks can reflect the change in RAC macroperformance.

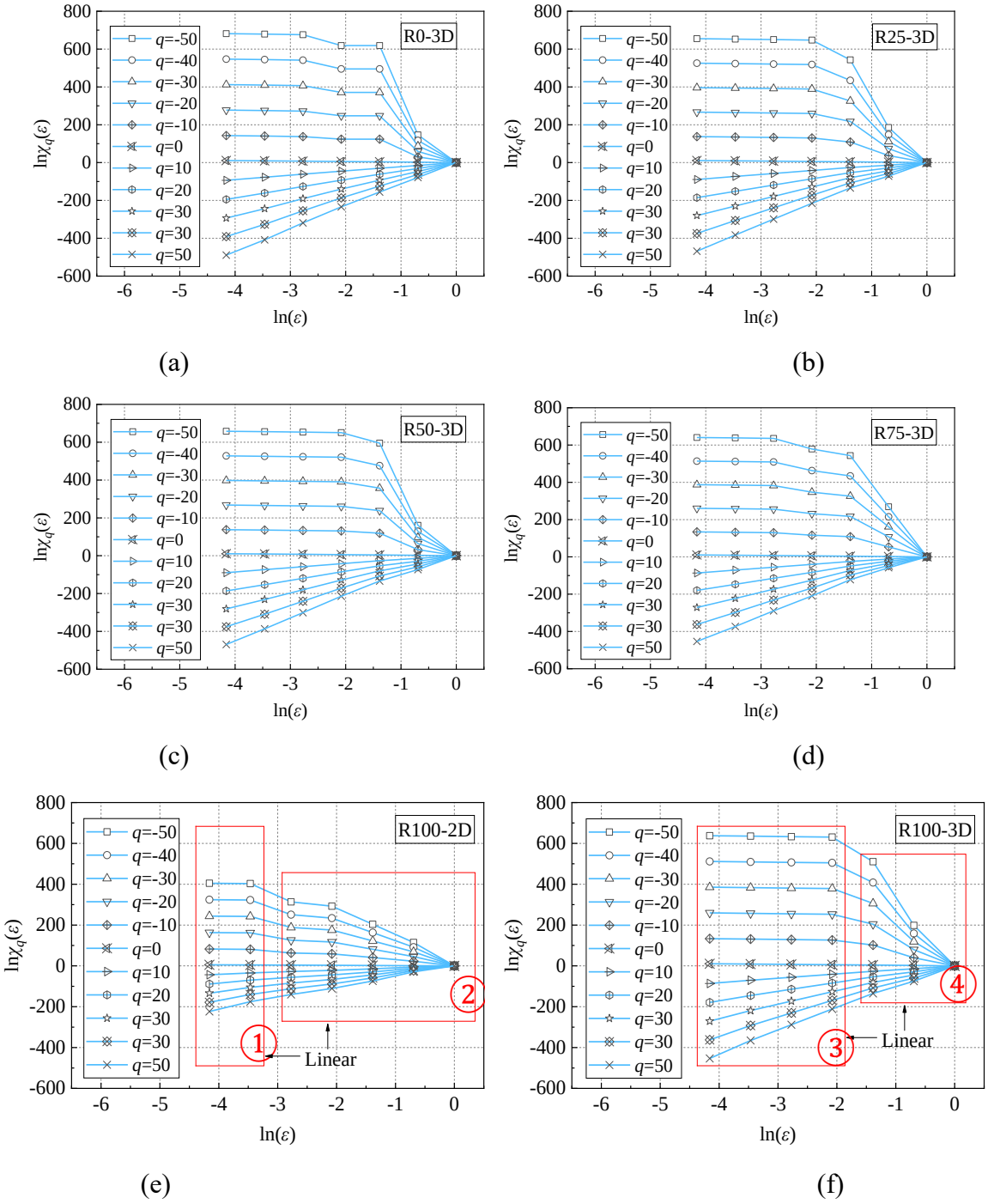

Fig. 13. $\ln\chi_q(\varepsilon)$-$\ln\varepsilon$ plots curves

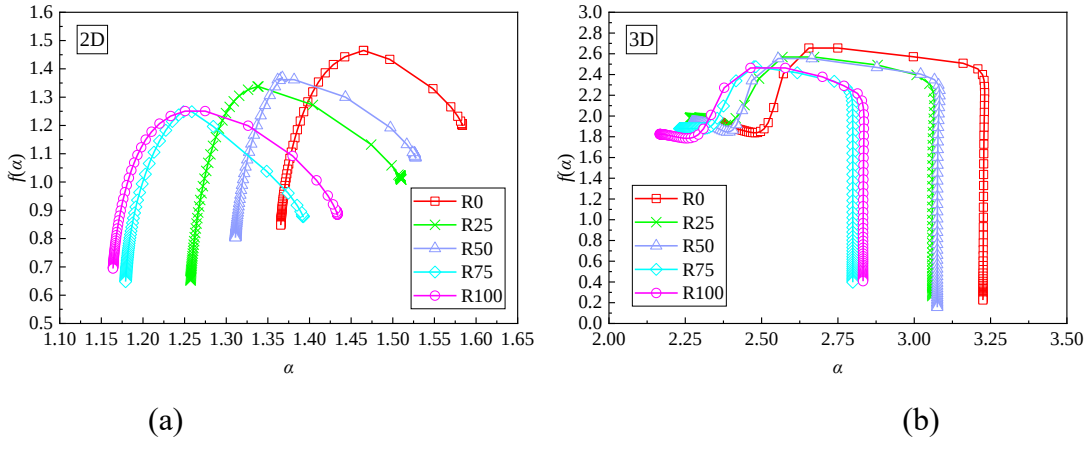

Fig. 14. Multifractal spectrum of mesocracks. (a) 2D images; (b) 3D structures.

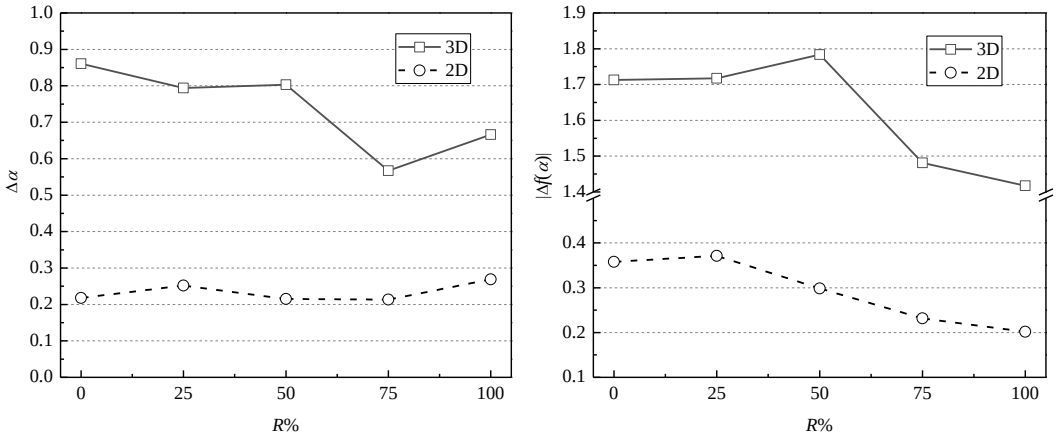

Fig. 15. Multifractal indicators of mesocracks in RAC with different RCA replacement rates

Table 4 Indicators of the multifractal spectrum of mesocracks.

Sample	△α(2D)	△$f(\alpha)$(2D)	△α(3D)	△$f(\alpha)$(3D)
R0	0.2180	0.3577	0.8606	-1.7127
R25	0.2517	0.3713	0.7938	-1.7173
R50	0.2151	0.2984	0.8029	-1.7838
R75	0.2131	0.2315	0.5669	-1.4810
R100	0.2690	0.2015	0.6660	-1.4173

4. Discussion

Aggregate characteristics have a significant impact on the mesostructure and macromechanical or durable properties of concrete **(Sáez del Bosquea et al., 2017; Shang et al., 2020b)**. The experimental results found that poor-quality RCA tend to release energy from themselves to trigger crack growth, thereby reducing the compressive strength of concrete. Weak particle strength provides a weak obstacle to crack propagation; therefore, the accumulation of less stress occurred around the position of aggregates, and less fracture energy was needed to advance the cracks. As a result, a smoother crack profile associated with a smaller fractal dimension was generated in RAC. On the other hand, the recycled aggregate-paste ITZ may become stronger due to the characteristics of RCA. The thickness of the recycled aggregates/paste ITZ is higher than that of the natural aggregates/paste ITZ **(Sáez del Bosquea et al., 2017)**. The water absorption of porous recycled aggregates may supply additional internal curing of the ITZ **(Li et al., 2020; Shang et al., 2020c)**. Thus, the double effects of weak particle strength and strong ITZ decrease the crack propagation for the RAC.

The results also indicate that the mesocrack characteristics inside concrete can be feasibly evaluated by the fractal method. By comparison, the traditional statistical method has to deal with

the numerous data of possible cracks. The fractal method combined with X-ray CT scanning technology could enhance the calculation efficacy, which can be a feasible pathway to bridge the micro- or mesostructure of concrete to its macromechanical or durable properties. In addition, using a single fractal indicator to reflect the geometric status of concrete simplifies the theoretical derivation based on mesomechanics. Although the branches and tortuosity of cracks decrease in the local area, the varieties of RCA properties and types bring uncertainty for crack propagation at the macroscale. Fractal characteristics try to describe the rule of mesocrack propagation at the spatial scale. The fractal dimension decreased with increasing RCA replacement rate; however, the variation in the fractal dimension from R25 to R50 was small, especially for the results obtained from the 3D structure. Thus, it is worth considering the spatial effects for research on crack propagation. The fractal and multifractal indicators can reflect the characteristics of the fractal body of concrete materials. During the calculation process, the box dimension algorithm constantly searches for the crack, and the characteristics accurately cover the fractal body at different scales. A small calculation scale is beneficial to capture the trend of the fractal body by the box dimension method. Thus, both the fractal dimension and multifractal spectrum are sensitive to the fractal body. The fractal difference of the cracks between 2D images and 3D structures indicates that 3D structures have one more dimension than 2D structures in Euclidean geometry. When the data points of the multifractal spectrum are crossed, they cannot be further analysed by a multifractal spectrum due to dropping out of a multifractal body (Ebrahimkhanlou et al., 2019), which occurs when the crack area is covered by 2-pixel boxes. Multifractal analysis is more sensitive than fractal analysis and provides a stricter definition of the fractal body.

Ideally, the fractal indicators of the mesocracks in 3D structures are assumed to be more representative of the true situation; however, they do not reflect the superiority in this study. In the fractal analysis, the self-similarities of the mesocracks are similar in 2D images and 3D structures. The fractal dimensions have a strong correlation with the RCA replacement rate. Both 2D images and 3D structures can obtain similar fractal dimensions of mesocrack growth. This also indicates that a significant relation exists between the surface crack characteristics and crack volume under the action of compressive loading. In the multifractal analysis, the spectrum stability in 3D structures is weaker than that in 2D images. This may be due to the information compatibility. In other words, although more mesocrack information is contained in 3D structures, its corresponding multifractal properties restrict the calculation. As a result, multifractal indicators from 2D images

are better than 3D structures. Thus, a test of self-similarity and scale invariance for the fractal body is necessary before using fractal and multifractal characterization to evaluate mesocrack growth.

5. Conclusions

The purpose of this study was to understand the development of interior mesocracks and the failure mechanism of RAC by using X-ray CT technology and image analysis. Digital matrix method-based fractal geometry theory and statistical methods were further applied to qualify these mesocracks as numerically extracted and restored in the form of 2D images and 3D structures. Four eigenvalues of the multifractal spectrum were used to reflect the evolution of the corresponding mesodamage. The following conclusions can be drawn:

- The interior mesocrack development path can be visually and qualitatively captured by X-ray CT scanning. The length, width, tortuosity, and density of the mesocrack can be measured through statistical methods, but it is not suitable for large-scale analysis due to the low efficiency. Mesocracks inside concrete have self-similarity characteristics, and the region is a multifractal body. Fractal geometry theory is an effective means to analyse the self-similarity of concrete materials by virtue of accurate coverage and intelligent calculation.
- RCA characteristics influence the mesocrack propagation pattern. As the RCA replacement rate increases, the length of the interior mesocracks increases, but the number, width, tortuosity, and density of the interior mesocracks decrease.
- A clear correlation exists between the fractal dimension and RCA replacement rate: the higher the RCA replacement rate is, the lower the fractal dimension, and the less tortuose the mesocracks. The multifractal spectrum effectively reflects the characteristics of mesofailure cracks at different levels from the local to the global level. However, multifractal analysis is more sensitive than fractal analysis as well as a stricter definition of the fractal body.
- The fractal dimension of mesocracks for concretes with different RCA replacement rates ranges from 2.39 to 2.18 based on 3D structures and 1.32 to 1.19 for 2D images. A similar drop in the fractal dimension occurred when NCA was replaced by RCA. No superiority is found in the fractal analysis from the 3D structure, although the statistical results indicate that the mesocrack characteristics from the 3D structure supply more accurate information than the description from 2D images.

Acknowledgements

We would like to acknowledge the financial support from the National Natural Science

Foundation of China (Project No: 51708091), and the Systematic Project of Guangxi Key Laboratory of Disaster Prevention and Engineering Safety (Grant No. 2019ZDK027).

References

Agrela, F., Díaz-López, J.L., Rosales, J., Cuenca-Moyano, G.M., Cano, H., Cabrera, M., 2021. Environmental assessment, mechanical behavior and new leaching impact proposal of mixed recycled aggregates to be used in road construction. J. Clean. Prod. 280, 124362.

Ahmed, H., Tiznobaik, M., Huda, S. B., Islam, M. S., Alam, M. S., 2020. Recycled aggregate concrete from large-scale production to sustainable field application. Constr. Build. Mater. 262, 119979.

Akhavan, A., Shafaatian, S., Rajabipour, F., 2012. Quantifying the effects of crack width, tortuosity, and roughness on water permeability of cracked mortars, Cem. Concr. Res. 42, 13-320.

Andreu, G., Miren, E., 2014. Experimental analysis of properties of high performance recycled aggregate concrete, Constr. Build. Mater. 52, 227–235.

Berger, F., Gauvin, F., Brouwers, H.J.H., 2020. The recycling potential of wood waste into wood-wool/cement composite, Constr. Build. Mater. 260, 119786.

Bai, G., Zhu, C., Liu, C., Liu, B., 2020. An evaluation of the recycled aggregate characteristics and the recycled aggregate concrete mechanical properties, Constr. Build. Mater. 240, 117978.

Brisarda, S., Serdarb, M., Monteiro, P. J. M., 2020. Multiscale X-ray tomography of cementitious materials: A review. Cem. Concr. Res. 128, 105824.

Butler, L., West, J.S., Tighe, S.L., 2011. The effect of recycled concrete aggregate properties on the bond strength between RCA concrete and steel reinforcement, Cem. Concr. Res. 41, 1037–1049.

Cantero, B., Bravo, M., de Brito, J., Sáez del Bosque, I.F., Medina, C, 2020. Mechanical behaviour of structural concrete with ground recycled concrete cement and mixed recycled aggregate. J. Clean. Prod. 275, 122913.

Carpinteri, A., 1994. Fractal nature of material microstructure and size effects on apparent mechanical properties, Mech. Mater. 18, 89-101.

Casuccio, M., Torrijos, M.C., Giaccio, G., Zerbino R., 2008. Failure mechanism of recycled aggregate concrete, Constr. Build. Mater. 22, 1500–1506.

Chiaia, B., Mier, J. G. M., Vervuurt, A., 1998. Crack Growth Mechanisms in Four Different Concretes: Microscopic Observations and Fractal Analysis, Cem. Concr. Res. 28, 103-114.

Ebrahimkhanlou, A., Athanasiou, A., Hrynyk, T.D., Bayrak, O., Salamone, S., 2019. fractal and multifractal analysis of crack patterns in prestressed concrete girders, J. Bridge Eng. 24, 04019059.

Erdem, S., Blankson, M.A., 2013. Fractal–fracture analysis and characterization of impact-fractured surfaces in different types of concrete using digital image analysis and 3D nanomap laser profilometery, Constr. Build. Mater. 40, 70–76.

Erdem, S. Hanbaya, S. Blankson. M. A., 2017. Self-sensing damage assessment and image-based surface crack quantification of carbon nanofibre reinforced concrete. Constr. Build. Mater. 134, 520–529.

Erdem, S., Gürbüz, E., Uysal, M., 2018. Micro-mechanical analysis and X-ray computed tomography quantification of damage in concrete with industrial by-products and construction waste. J. Clean. Prod. 189, 933-940.

Falconer, K., 2003. Fractal geometry: Mathematical foundations and application, Wiley, New York.

Ficker, T., 2012. Fracture surfaces and compressive strength of hydrated cement pastes, Constr. Build. Mater. 27, 197–205.

GB/T 14685-2011: Pebble and crushed stone for construction. General Administration of Quality Supervision, Inspection and Quarantine of the People's Republic of China, Beijing, China.

GB/T 25177-2010: Recycled coarse aggregates for concrete. General Administration of Quality Supervision, Inspection and Quarantine of the People's Republic of China, Beijing, China.

GB/T 50081-2002: Standard for test method of mechanical properties on ordinary concrete. Ministry of Construction of the People’s Republic of China, Beijing, China.

Gupta,T., Siddique, S., Sharma, R. K., Chaudhary, S., 2019. Behaviour of waste rubber powder and hybrid rubber concrete in aggressive environment, Constr. Build. Mater. 217, 283-291.

Golewski, G. L., 2018. Evaluation of morphology and size of cracks of the Interfacial Transition Zone (ITZ) in concrete containing fly ash (FA), J. Hazard. Mater. 357, 298-304.

Han, T. S., Zhang, X., Kim, J.S., Chung, S.Y., Lim, J.H., Linder, C., 2018. Area of linealpath function for describing the pore microstructures of cement paste and their relations to the mechanical properties simulated from l-CT microstructures, Cem. Concr. Compos. 89,1–17.

Huang Y. J., Yang Z. J., Ren W. Y., Liu G. H., Zhang C. Z., 2015. 3D meso-scale fracture modelling and validation of concrete based on in-situ X-ray Computed Tomography images using damage plasticity model. Int. J. Solids. Struct. 67–68, 340–352.

Issa. M. A., Hammad, M., 1993. Fractal characterization of fracture surfaces in mortar, Cem. Concr. Res. 23 (1993) 7-12.

Jalilifar, H., Sajedi, F., 2020. Micro-structural analysis of recycled concretes made with recycled coarse concrete aggregates. Constr. Build. Mater. 121041.

Jayasuriya, A., Shibata, E. S., Chen T., Adams, M. P., 2021. Development and statistical database analysis of hardened concrete properties made with recycled concrete aggregates, Resour. Conserv. Recycl. 164,105121.

Koper, A., Koper, W., Koper, M., 2017. Influence of Raw Concrete Material Quality on Selected Properties of Recycled Concrete Aggregates. Procedia Eng. 172, 536-543.

Kumar, S., Barai, S. V., Concrete fracture models and applications. 1st ed. Berlin, 2011.

Lange, D. A., Jennings, H. M., Shah, S., 1993. Relationship between fracture roughness and fracture behavior of cement paste and mortar, J. Am. Ceram. Soc. 76, 589-597.

Li Z., Hao P., Liu H., Xu J. 2019, Effect of cement on the strength and microcosmic characteristics of cold recycled mixtures using foamed asphalt. J. Clean. Prod. 230, 956-965.

Li, Z., Liu, J., Xiao, J., Zhong P, 2020. Internal curing effect of saturated recycled fine aggregates in early-age mortar, Cem. Concr. Compos. 108, 103444.

Liu, B., Ma, R., Fan, H., 2021. Evaluation of the impact of freeze-thaw cycles on pore structure characteristics of black soil using X-ray computed tomography. Soil Tillage Res. 206,104810.

Liu, J. H., Jiang, R. N., Sun, J. H., Shi, P. F., Yang Y. F., 2017. Concrete damage evolution and three-dimensional reconstruction by integrating CT test and fractal theory, J. Mater. Civ. Eng. 29, 04017122.

Liu, Q., Xiao, J. Z., Sun, Z.H., 2011. Experimental study on the failure mechanism of recycled concrete, Cem. Concr. Res. 41, 1050–1057.

Morgan, I. L., Ellinger, H., Klinksiek, R., Thompson, J.N., 1980. Examination of concrete by computerized tomography, J. Am. Con. Ins. 77 23–27.

Nayak, S. R. Mishra, J., Palai, G., 2018. A modified approach to estimate fractal dimension of gray scale images, Optik 161, 136–145.

Nežerka, V., Bílý, P., Hrbek,V., Fládr, J., 2019, Impact of silica fume, fly ash, and metakaolin on the thickness and strength of the ITZ in concrete. Cem. Concr. Compos. 103, 252-262

Nitka, M., Tejchman, J., 2018. A three-dimensional meso-scale approach to concrete fracture

based on combined DEM with X-ray μ CT images. Cem. Concr. Res. 107, 11–29.

Oliveira, T.C.F., Dezen, B.G.S., Possan, E., 2020. Use of concrete fine fraction waste as a replacement of Portland cement. J. Clean. Prod. 273, 123126.

Ouyang, K., Shi, C., Chu, H., Guo, H., Song, B., Ding, Y., Guan, X., Zhu, J., Zhang, H., Wang, Y., Zheng, J., 2020. An overview on the efficiency of different pretreatment techniques for recycled concrete aggregate. J. Clean. Prod. 263, 121264.

Sáez del Bosquea, I. F., Zhu, W., Howind, T., Matías, A., Sánchez de Rojasc, M. I., Medina, C., 2017. Properties of interfacial transition zones (ITZs) in concrete containing recycled mixed aggregate, Cem. Concr. Compos. 81 (2017) 25-34

Saouma, V. E., Barton, C. C., Gamaleldin, N. A., 1990. Fractal characterization of fracture surfaces in concrete, Eng. Fract. Mech. 35, 47-53.

Skarżyński, Ł., Tejchman, J., 2019. Experimental investigations of damage evolution in concrete during bending by continuous micro-CT scanning. Mater. Charact. 154, 40-52.

Shang, X. Y, Li, J. S., 2020a. Manufacturing and performance of environment-friendly lightweight aggregates with core-shell structure, J. Clean. Prod. 276, 123157.

Shang, X. Y., Li, J. S., Zhan, B. J., 2020b. Properties of sustainable cellular concrete prepared with environment-friendly capsule aggregates. J. Clean. Prod. 267, 122018.

Shang, X. Y., Zhan, B. J., Li, J. S., Zhong, R., 2020c. Novel microcapsules for internal curing of high-performance cementitious system. Sci. Rep. 10, 8318.

Tarquis, A. M., Heck, R. J., Andina, D., Alvarez, A., Antón, J. M, 2009. Pore network complexity and thresholding of 3D soil images, Ecol. Complexity 6, 230-239.

Tian, W. Han, N., 2019. Evaluation of meso-damage processes in concrete by X-Ray CT scanning techniques under real-time uniaxial compression testing, J. Nondestr. Eval. 38, 44.

Trtik, P., Diaz, A., Guizar-Sicairos, M., Menzel A., 2013. O. Bunk, Density mapping of hardened cement paste using ptychographic X-ray computed tomography, Cem. Concr. Compos. 36, 71–77.

Wang, P., Qiao, H., Zhang, Y., Li, Y., Feng, Q. Chen, K., 2020. Meso-damage evolution analysis of magnesium oxychloride cement concrete based on X-CT and grey-level co-occurrence matrix. Constr. Build. Mater. 255, 119373.

Wei, D., Hurley, R. C., Poh L. H., Dias-da-Costa, D., Gan, Y., 2020. The role of particle morphology on concrete fracture behaviour: A meso-scale modelling approach. Cem. Concr. Res.

134, 106096.

Winslow, D. N, 1985. The fractal nature of the surface of cement paste, Cem. Concr. Res. 15, 817–824.

Wu, Y. C., Xiao, J. Z., 2018. The effect of microscopic cracks on chloride diffusivity of recycled aggregate concrete, Constr. Build. Mater. 170, 326–346.

Wu, Z., Wong, H.S., Buenfeld, N.R., 2015. Influence of drying-induced microcracking and related size effects on mass transport properties of concrete, Cem. Concr. Res. 68, 35–48.

Xiao, R., Polaczyk, P., Jiang, X., Zhang, M., Wang, Y., Huang, B., 2021. Cementless controlled low-strength material (CLSM) based on waste glass powder and hydrated lime: Synthesis, characterization and thermodynamic simulation,Constr. Build. Mater. 275, 122157.

Xiao, R., Polaczyk, P., Zhang, M., Jiang, X., Zhang, Y., Huang, B., Hu, W., 2020. Evaluation of glass powder-based geopolymer stabilized road bases containing recycled waste glass aggregate, Transp. Res. Rec. 2674(1), 22-32.

Xu, Y., Qian, C., Pan, L., Wang, B., Lou, C., 2012. Comparing monofractal and multifractal analysis of corrosion damage evolution in reinforcing bars. PLoS ONE 7, 1–8.

Yang, X., Wang, F. L., Yang, X.C., Zhou, Q, 2017. Fractal dimension in concrete and implementation for meso-simulation, Constr. Build. Mater. 143, 464–472.

Zhang, H., Šavija, B., Lukovic, M., Schlangen, E., 2019. Experimentally informed micromechanical modelling of cement paste: an approach coupling X-ray computed tomography and statistical nanoindentation, Compos. Pt. B-Eng. 157, 109–122.

Zhang, H., Wei, D., 2010. Estimation of fracture toughness, driving force, and fracture energy for fractal cracks using the method of imaginary smooth crack, Eng. Fract. Mech. 77 (2010) 621–630.

Zhang, M., Jivkov, A., 2016. Micromechanical modelling of deformation and fracture of hydrating cement paste using X-ray computed tomography characterisation, Compos. Pt. B-Eng. 88, 64–72.

Zhou, J., He, X., Zhang, L., 2020. CT characteristic analysis of sea-sand concrete exposed in simulated marine environment. Constr. Build. Mater. 121170.